

# Wafer-Scale Lateral Self-Assembly of Mosaic $\text{Ti}_3\text{C}_2\text{T}_x$ MXene Monolayer Films

Mehrnaz Mojtabavi, Armin Vahid Mohammadi, Karthik Ganeshan, Davoud Hejazi, Sina Shahbazmohamadi, Swastik Kar, Adri C. T. van Duin, and Meni Wanunu\*



Cite This: <https://dx.doi.org/10.1021/acsnano.0c06393>



Read Online

ACCESS |



Metrics & More



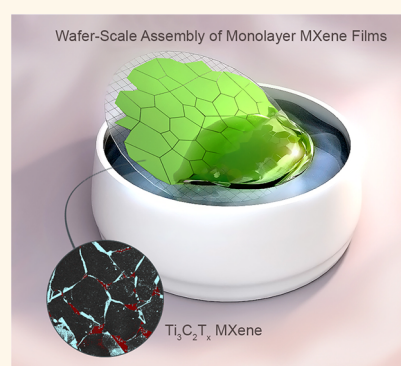
Article Recommendations



Supporting Information

**ABSTRACT:** Bottom-up assembly of two-dimensional (2D) materials into macroscale morphologies with emergent properties requires control of the material surroundings, so that energetically favorable conditions direct the assembly process. MXenes, a class of recently developed 2D materials, have found new applications in areas such as electrochemical energy storage, nanoscale electronics, sensors, and biosensors. In this paper, we present a lateral self-assembly method for wafer-scale deposition of a mosaic-type 2D MXene flake monolayer that spontaneously orders at the interface between two immiscible solvents. ReaxFF molecular dynamics simulations elucidate the interactions of a MXene flake with the solvents and its stability at the liquid/liquid interface, the prerequisite for MXene flakes self-assembly at the interface. Moreover, facile transfer of this monolayer onto a flat substrate (Si, glass) results in high-coverage monolayer films with uniform thickness and homogeneous optical properties. Multiscale characterization of the resulting films reveals the mosaic structure and sheds light on the electronic properties of the films, which exhibit good electrical conductivity over cm-scale areas.

**KEYWORDS:** self-assembly, MXene, 2D materials, 2D titanium carbide, monolayer, conductive



In recent years, various types of two-dimensional (2D) materials have gained much attention due to their emergent properties and have played significant roles in the development of new types of electrical devices,<sup>1–3</sup> chemical/biological sensors,<sup>4–7</sup> water purification membranes,<sup>8,9</sup> energy conversion/storage devices,<sup>1,10,11</sup> and other products. Despite widespread theoretical and experimental research into the physics and applications of 2D materials, a practical challenge common to all of these materials is related to their handling, where their extremely thin nature and ultrahigh aspect ratios (1000–10,000) demand methods for manipulation and assembly of these materials during device manufacturing. For example, in applications where a controlled 2D material film is required for harvesting the material's electrical and optical properties over macroscale areas, techniques for large-scale assembly of 2D flakes into uniform mono- and multilayer films are in need. Efforts to address this ongoing challenge have resulted in the development of several large-scale thin-membrane assembly methods. These methods can be categorized into two groups: (1) assembly of ultrathin films from a 2D material flake dispersion, either directly on a substrate or at an interface (liquid/liquid or liquid/air),<sup>12,13</sup> and (2) direct large-area chemical vapor deposition (CVD) of 2D materials on a substrate, followed by use or transfer to another substrate.<sup>14,15</sup>

Among 2D materials, graphene oxide (GO) and its reduced counterpart (rGO) have been widely studied for large-scale monolayer film assembly from their dispersions. Precise methods for casting uniform layers of GO/rGO on substrates include the Langmuir method,<sup>16–21</sup> spin-coating,<sup>19,22,23</sup> and layer-by-layer assembly.<sup>24,25</sup> The Langmuir and spin-coating methods result in well-packed films with organized structure and controlled thickness,<sup>23</sup> while other methods result in a looser, more disordered structure.<sup>12</sup> For other 2D materials such as graphene,  $\text{MoS}_2$ , and  $\text{WS}_2$ , poor stability in water and other common solvents limits the quality of their assembly into a film from a dispersion phase.<sup>26–28</sup> Their wafer-scale CVD synthesis, however, has been shown to result in more uniform and reproducible films.<sup>29–35</sup>

2D transition metal carbides and nitrides (MXenes) as an emerging class of electrically conductive, hydrophilic, and optically active 2D materials have been subjects of numerous

**Received:** July 30, 2020

**Accepted:** December 29, 2020

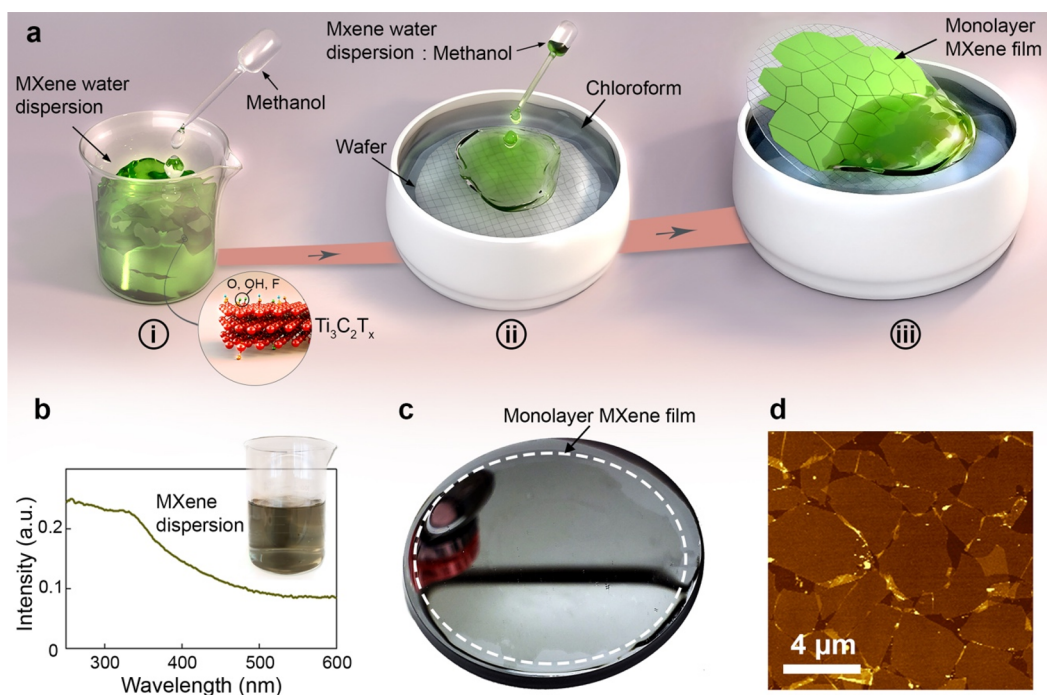


**Figure 1.** Lateral self-assembly of  $\text{Ti}_3\text{C}_2\text{T}_x$  MXene flakes at a liquid/liquid interface and transfer on a substrate. (a) Schematic illustration of self-assembly and transfer steps of monolayer  $\text{Ti}_3\text{C}_2\text{T}_x$  film. The atomic structure of  $\text{Ti}_3\text{C}_2\text{T}_x$  MXene is shown with  $\text{O}^-$ ,  $\text{OH}^-$ , and  $\text{F}^-$  as functional groups on the surface. (b) UV-vis absorbance spectrum of diluted  $\text{Ti}_3\text{C}_2\text{T}_x$  dispersion optimized for assembly of monolayer flakes at the liquid/liquid interface. (c) Optical image of a 3 in. Si wafer coated with a monolayer  $\text{Ti}_3\text{C}_2\text{T}_x$  film. The white dashed circle highlights the approximate edges of the transferred film. (d) AFM image of a  $\text{Ti}_3\text{C}_2\text{T}_x$  monolayer film after transfer on a  $\text{SiN}_x$  substrate.

studies in recent years.<sup>2,36</sup> Their synthesis from MAX phases, in which the MXene layers are bound together by group 13 elements such as Al, Si, *etc.* (A layer in MAX phase structure), is well established and involves selective etching of the A elements and MXene exfoliation in aqueous fluorine-containing acidic solutions.<sup>2</sup> The resulting MXenes have a general formula of  $\text{M}_{n+1}\text{X}_n\text{T}_x$  where M is a transition metal, X is carbon/nitrogen,  $n$  can be 1, 2, 3, or 4, and  $\text{T}_x$  represents oxygen, hydroxyl, and fluorine groups present on the MXene basal planes. Assembly and fabrication of ultrathin (*i.e.*, monolayer) MXene films, however, have so far been challenging and limited the implementation of these materials into devices that require nanometer-thick membranes. Layer-by-layer assembly<sup>37</sup> has shown potential for controlled assembly of MXene monolayer and multilayer films, and other methods have been employed for MXene assembly into thin films, including spin coating,<sup>38</sup> spray coating,<sup>39,40</sup> and dip coating.<sup>41</sup> Recently, an interfacial assembly method was used for assembling  $\text{Ti}_3\text{C}_2\text{T}_x$  MXene layers at an air/water interface, assisted by ethyl acetate.<sup>42,43</sup> However, in this work, the number of layers varied significantly during deposition, possibly due to strong convection induced by rapid ethyl acetate evaporation. Also, Pethukhov *et al.*<sup>44</sup> and Kim *et al.*<sup>45</sup> reported MXene monolayer assembly at the liquid/air interface using the Langmuir–Blodgett and Langmuir–Schaefer techniques, respectively. In these works, surface pressure was controlled using a movable barrier at the air–water interface to direct close contact between flakes and achieve various levels of packing and overlap. However, these methods require precise control of film area and substrate positioning to direct the flake organization and to facilitate transfer to substrates.

We recently developed a method for lateral self-assembly of MXenes at a liquid/liquid interface to fabricate monolayer to

multilayer  $\text{Ti}_3\text{C}_2\text{T}_x$  and  $\text{Ti}_2\text{CT}_x$  MXene films over mm-sized areas and used them as nanometer-thin freestanding membranes in solid-state nanopore sensing applications.<sup>46</sup> Herein, we have further refined our rapid interfacial self-assembly technique to enable large-scale fabrication of monolayer to few-layer  $\text{Ti}_3\text{C}_2\text{T}_x$  films with control over the nominal film thickness, flake density, and lateral size of the self-assembled films. We find that careful control over the MXene suspension concentration affords large-area films with high monolayer coverage and <10% void areas, as characterized by transmission electron microscopy (TEM), scanning electron microscopy (SEM), and atomic force microscopy (AFM) techniques as well as Raman mapping and ellipsometric mapping. Further, successive depositions of monolayer films result in bilayers and trilayers as indicated by optical transmission spectra and electrical sheet resistance measurements. Moreover, to investigate the mechanism and parameters involved in this self-assembly process, we used ReaxFF molecular dynamics (MD) simulations, the result of which showed how the interaction of a MXene flake with the solvents render its stability at the liquid/liquid interface.

Our lateral self-assembly method results in rapid formation of mosaic-type high-coverage monolayer MXene films without the need for any specialized instrumentation. This simple approach facilitates device fabrication for applications that require large-area uniform MXene films.

## RESULTS AND DISCUSSION

We synthesized  $\text{Ti}_3\text{C}_2\text{T}_x$  MXene from its MAX phase ( $\text{Ti}_3\text{AlC}_2$ ) according to the MILD synthesis method<sup>47</sup> (see [Materials and Methods](#) section for details). Previously, we showed using  $\text{Ti}_3\text{C}_2\text{T}_x$  and  $\text{Ti}_2\text{CT}_x$  MXenes that liquid/liquid interfacial self-assembly can be used to generate large-area

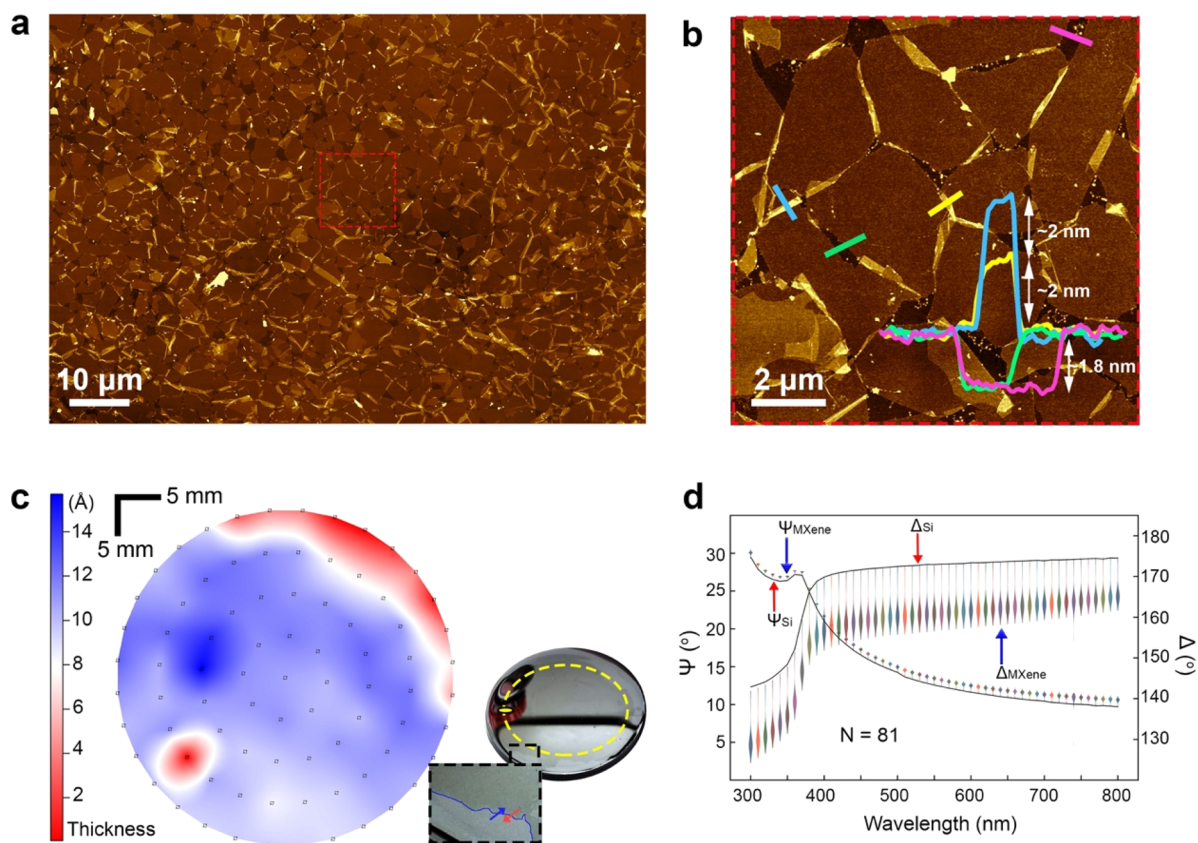


**Figure 2.** Characterization of monolayer  $\text{Ti}_3\text{C}_2\text{T}_x$  film uniformity. (a) Large area ( $100 \times 70 \mu\text{m}^2$ ) AFM image produced by stitching together 12 individual images for a  $\text{Ti}_3\text{C}_2\text{T}_x$  monolayer film after transfer onto a  $\text{Si}/\text{SiN}_x$  substrate. (b) AFM image of the dashed red area shown in (a) with corresponding line profiles. (c) Ellipsometric mapping of  $\text{Ti}_3\text{C}_2\text{T}_x$  monolayer film transferred onto a 3 in. Si wafer, shown on the right. The yellow dashed circle shows the area (with 4 cm diameter) within which ellipsometric mapping was carried out. The yellow oval shape shows the approximate shape and size of the incident beam. The magnified image of the black dashed square shows the edges of the  $\text{Ti}_3\text{C}_2\text{T}_x$  film on the Si substrate. The blue arrow shows the film, and the red arrow shows the bare substrate. (d) Violin plots of obtained  $\Psi$  and  $\Delta$  values from 81 points in a circular area of a transferred  $\text{Ti}_3\text{C}_2\text{T}_x$  film (shown with blue arrows). The red arrows show the  $\Psi$  and  $\Delta$  values obtained from the bare Si wafer.

suspended flake assemblies, which facilitates transfer onto substrates without the need for alignment of the flake and the substrate feature (e.g., nanoaperture). We transferred the free-standing MXene films onto  $\text{SiN}_x$  membranes ( $\sim 50$  nm thick) with prefabricated  $\sim 100$  nm nanoapertures, and used them as support membranes for nanoscale pores for single-molecule biopolymer sensing.<sup>46</sup> Upon applying a voltage across the pore, nearly no ionic current leakage was observed through free-standing MXene films without any pores, which demonstrated excellent adhesion of MXene films on their respective substrates. In a more recent study, Li *et al.*<sup>48</sup> reported the adhesion energy of  $\text{Ti}_3\text{C}_2\text{T}_x$  MXene to Si substrate is  $0.90 \pm 0.03 \text{ J m}^{-2}$ , which is of the same order of magnitude as for graphene monolayers. In the current study, we refined and scaled-up our approach to the wafer-scale assembly process, as schematically illustrated in Figure 1a. After chemical exfoliation of  $\text{Ti}_3\text{C}_2\text{T}_x$  and delamination of the monolayer flakes in water, we diluted the dispersion to an optimal concentration for monolayer assembly controlled by UV-vis absorbance spectrometry (Figure 1b) using an Eppendorf BioSpectrometer (New York, USA). It is crucial for the dispersion concentration to be optimized for the self-assembly process: If the dispersion is too concentrated, a multilayer film with non-uniform thickness will form, while a diluted dispersion results in a less packed monolayer film and small coverage areas. Then, we

added methanol to the MXene dispersion to a volume ratio of 1:8 methanol:water (step (i)). Next, we submerged the substrate of interest in a chloroform bath in a PTFE dish and drop cast a few droplets of the prepared mixed dispersion on top of the chloroform to initiate the self-assembly process (step (ii)). Immediately following this, flakes begin to coalesce at the chloroform/water interface, forming a large-area two-dimensional film within 5–10 min depending on the final film dimensions. Once assembled, as visualized by no increase in the overall size of the assembly, the film is transferred to the substrate by slowly lifting the substrate from the bottom of the chloroform bath in a way that the film rests on top of the substrate and then placing the substrate on a hot plate, with the whole lifting process taking about 1–2 min (step (iii)). This is followed by drying on a hot plate at  $100^\circ\text{C}$  for 30 min to ensure MXene:substrate adhesion and complete the transfer process. Supplementary Movie S1 shows the  $\text{Ti}_3\text{C}_2\text{T}_x$  film assembly and transfer onto a  $25 \times 40 \text{ mm}^2$  glass microscope slide in detail, with the whole process taking about 12 min. To facilitate visualization we used a dispersion with a relatively higher concentration, as well as a transparent substrate. Also, Supplementary Movie S2 shows that after mechanical disruption of the self-assembled film structure, the flakes rearrange again to restore their ordered structure. Depending on the desired application or characterization method, different

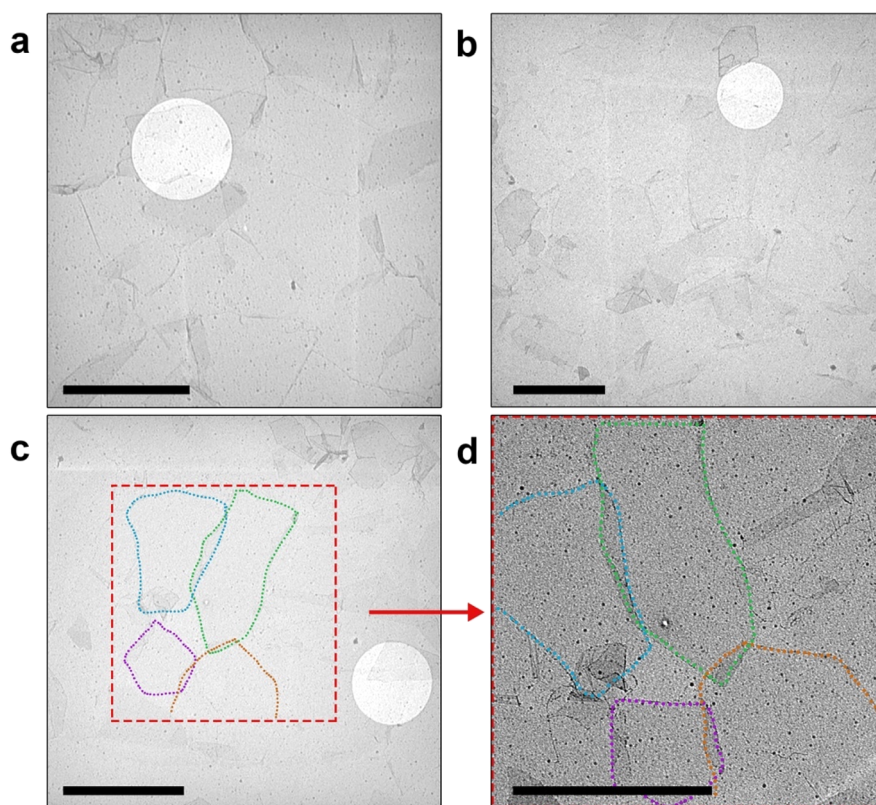


**Figure 3.** (a–d) Bright-field TEM images of a transferred monolayer  $\text{Ti}_3\text{C}_2\text{T}_x$  films on a freestanding 50 nm-thick  $\text{SiN}_x$  membrane. The  $\sim 3 \mu\text{m}$  bright circle is a  $\sim 30$  nm-thick thin region within the membrane. All scale bars = 5  $\mu\text{m}$ .

substrate types and sizes could be used. However, hydrophobic surfaces such as  $\text{SiN}_x$  and HOPG require further surface treatment such as piranha cleaning, oxygen plasma, or UV/ozone cleaning to render the surface more hydrophilic. In Figure 1c, we present an optical image of a 3 in. Si wafer onto which we deposited a monolayer of  $\text{Ti}_3\text{C}_2\text{T}_x$  film. The optical image shows a covered wafer before the water completely evaporated. The dashed white circle highlights the approximate edges of the transferred film, which provides an optical contrast from the bare, uncovered Si substrate. Figure 1d shows an AFM image of monolayer  $\text{Ti}_3\text{C}_2\text{T}_x$  film after transfer onto a  $\text{SiN}_x$  substrate, demonstrating the mosaic structure of the film.

To investigate the properties of the fabricated films and their potential applications, we studied structure, uniformity, fractional area of coverage, and optical and electrical properties of the fabricated films. Figure 2a shows a stitched image of 12 individual AFM images obtained on a monolayer  $\text{Ti}_3\text{C}_2\text{T}_x$  film transferred onto a  $\text{SiN}_x$  substrate. This image confirms long-range, well-packed, and edge-to-edge flake arrangements with partial overlaps at the flake-to-flake boundaries. Figure S1 shows six different  $30 \times 30 \mu\text{m}^2$  area AFM images from the stitched image in Figure 2a with corresponding height profiles. Average surface roughness values within the  $30 \times 30 \mu\text{m}^2$  area are in the range of 1.2–1.7 nm, which indicates the smooth nature of the monolayer films. Figure 2b shows a magnified AFM image of the dashed red area in Figure 2a with the corresponding line height profile of monolayer flakes. The thickness of a monolayer  $\text{Ti}_3\text{C}_2\text{T}_x$  flake is measured around 1.8 nm (see also Figure S2). Theoretically, the thickness of a  $\text{Ti}_3\text{C}_2\text{T}_x$  flake is 0.98 nm; however, height artifacts in AFM are common for hydrophilic materials due to the presence of water beneath/above the flake, presence of functional groups on the

MXene basal plane, and interactions of the bound surface groups of  $\text{Ti}_3\text{C}_2\text{T}_x$  flakes with the substrate, all resulting in a typical AFM-based thickness of 1.5–2 nm for  $\text{Ti}_3\text{C}_2\text{T}_x$  monolayer flakes,<sup>49,50</sup> in agreement with our measurements. This figure also shows two line-height profiles at the edges (blue and yellow lines) where flakes fold onto each other and form wrinkles. These profiles show heights of 2 and 4 nm from the surface of the flakes. To further corroborate the monolayer film thickness, we performed ellipsometric measurements. In Figure 2c, we demonstrate an ellipsometric thickness map of a monolayer  $\text{Ti}_3\text{C}_2\text{T}_x$  film deposited on a 3 in. Si wafer. The optical image of the wafer on the right shows a dashed yellow circle (4 cm in diameter) within which an 81-point ellipsometric mapping routine was carried out, and the yellow oval shape on the image roughly represents the size/shape of the ellipsometric incident light beam ( $\sim 1.2$  mm beam diameter). To assess the thickness variation across the wafer, we mapped the ellipsometric quantities  $\Psi$  and  $\Delta$  as a function of wavelength at all mapping points along the wafer. Using these data and published optical data for real ( $n$ ) and imaginary ( $k$ ) refractive indices for a  $\text{Ti}_3\text{C}_2\text{T}_x$  film for various wavelengths (see Figure S3),<sup>38,51</sup> we constructed a three-layer model of our sample (Si,  $\text{SiO}_2$ , and MXene layer) and fit our mapping data to produce a color map using Voronoi interpolation that represents the MXene layer thickness (see Materials and Methods section for more details). The areas covered with film show thickness values in the range of 0.9–1.5 nm, which we speculate corresponds to monolayer  $\text{Ti}_3\text{C}_2\text{T}_x$  film along with some areas containing partial bilayer due to laterally overlapping flakes in the assembly. The small value of the goodness-of-fit ( $\chi^2$ ) for each point on the wafer (Figure S4) demonstrates a good representation of optical constants

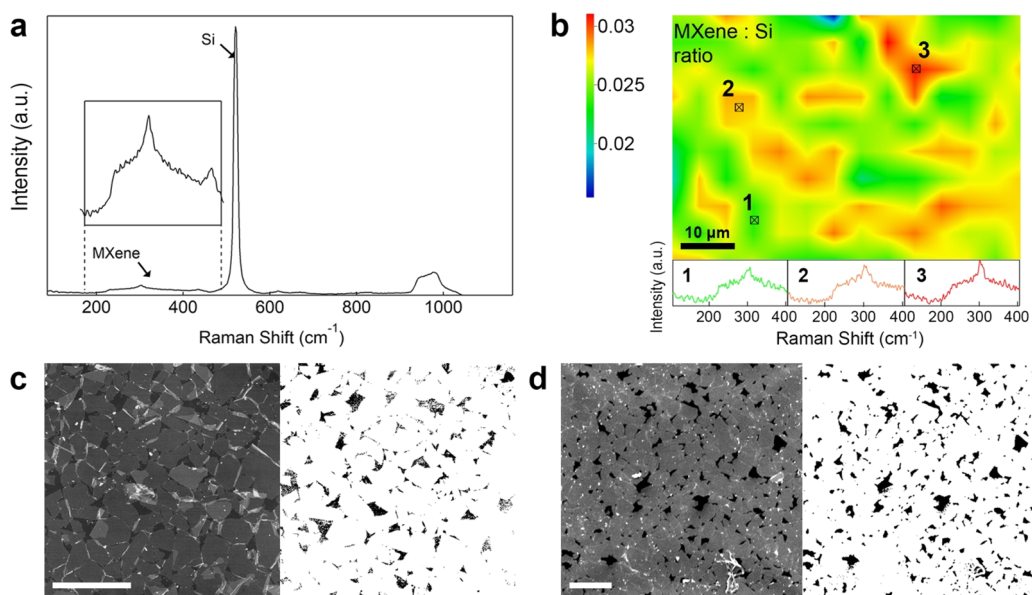


**Figure 4.** Characterization of monolayer  $\text{Ti}_3\text{C}_2\text{T}_x$  films coverage on a substrate. (a) Raman spectrum obtained from a monolayer  $\text{Ti}_3\text{C}_2\text{T}_x$  film on  $\text{Si}/\text{SiO}_2$  substrate. The strong peak of  $\text{Si}$  at  $521\text{ cm}^{-1}$  originates from the substrate. (b) Raman mapping of peak height ratio of MXene:  $\text{Si}$  for a  $68.5 \times 44.5\ \mu\text{m}^2$  area. The corresponding Raman spectra of points 1, 2, and 3 on the map are shown at the bottom of the image. (c) Left: AFM image of the transferred monolayer  $\text{Ti}_3\text{C}_2\text{T}_x$  film on a  $\text{SiN}_x$  substrate: Right: Analyzed image using ImageJ software showing 92.8% coverage of substrate by the film. (d) Left: SEM image of a transferred monolayer  $\text{Ti}_3\text{C}_2\text{T}_x$  film on 50 nm-thick freestanding  $\text{SiN}_x$  membrane: Right: Analyzed image using ImageJ software showing 91.8% coverage of substrate by the film. All scale bars =  $10\ \mu\text{m}$ , and black areas represent uncovered areas in all bottom images.

and thickness of the sample. The points on the wafer where the thickness is calculated  $<0.8\ \text{nm}$  have relatively higher  $\chi^2$  values. At these points, the measured  $\Psi$  and  $\Delta$  values do not fit the model very well (Figure S4), which we assume is due to lack of coverage of the film at these points. For a deeper insight into the quality of the ellipsometric data, we show in Figure 2d violin plots of  $\Psi$  and  $\Delta$  values measured at different points on the mapping experiment in Figure 2c and compare these with values for a bare  $\text{Si}$  substrate. The difference between  $\Psi$  and  $\Delta$  values for these two substrates confirms the presence of the film over the entire area of the wafer. For each wavelength measured, we find a normally distributed variation in  $\Psi$  and  $\Delta$  values for the MXene monolayer film. An analogous map of the measured  $\text{SiO}_2$  thickness is shown in Figure S5. Moreover, the outliers in the violin plots fit the data for bare  $\text{Si}$  substrate, which identifies a few uncovered regions on the wafer (Figure 2c, red arrow on the wafer and red region on the map). In another effort to interpret the experimental data from ellipsometry measurement, we used the effective medium approximation (EMA) model to describe the MXene layer as the mixture of the material (MXene) and void (air) (see Materials and Methods section for details). Fitting the data to this model determined the most pronounced film thickness and the fractional coverage of the MXene film with that thickness at each measured point on the wafer. Figure S6 shows the scatter plot of thickness *vs* coverage and the histogram of each parameter, indicating a  $\sim 20\ \text{\AA}$ -thick MXene film with  $\sim 70\%$  coverage over the measured wafer area, with only a few outliers. We speculate that the narrow regions where overlaps occur ( $\sim 200\ \text{nm}$  wide typically) are not properly measured by the ellipsometer beam, and thus the fractional coverage value is underestimated. Notably, this ellipsometric result agrees well with the measured MXene monolayer

fractional area ( $\sim 75\%$ ) calculated from the AFM images, as shown later.

To inspect the quality and cleanliness of our transfer process and elucidate the structure of the films at overlaps, we characterized the monolayer  $\text{Ti}_3\text{C}_2\text{T}_x$  films using TEM. To do so, we transferred MXene monolayers onto  $5 \times 5\ \text{mm}^2$   $\text{Si}$  chips hosting freestanding 50 nm-thick silicon nitride ( $\text{SiN}_x$ ) membranes at their centers. Figure 3a–c shows TEM images of monolayer films on  $\text{SiN}_x$  membrane. These images support that our transfer process results in a clean surface with high-quality film and uniform contrast, confirming the single-layer nature of the film. The region within the  $\text{SiN}_x$  membrane that was further thinned down to  $\sim 30\ \text{nm}$  appears as the bright round area, creating a “nano-step” feature on the membrane. Despite this feature on the surface, the flakes transferred onto the substrate in that region are not “wrapped”, and the integrity of the film has remained. Figure 3d shows a magnified image of the red dashed area in Figure 3c with the edges of four overlapping flakes highlighted with four different colors. The magnified image shows that at the overlapping regions, flakes are minimally overlaid on one another near the flakes’ edges, rather than being folded or crumbled. An unannotated version of Figure 3 (no boundary lines) is provided in Figure S7.

Another method to assess the coverage and uniformity of  $\text{Ti}_3\text{C}_2\text{T}_x$  films on a substrate is Raman spectroscopy. Sarycheva *et al.*<sup>52</sup> recently showed that the Raman spectrum of a single  $\text{Ti}_3\text{C}_2\text{T}_x$  flake has two characteristic peaks and, further, observed an increase in peak intensities upon multilayer stacking of these flakes. Unlike transition-metal dichalcogenides, multilayer  $\text{Ti}_3\text{C}_2\text{T}_x$  flakes did not show any peak shifts, which relates to the substantial interlayer gap that exists between MXene sheets ( $\sim 5\text{--}6\ \text{\AA}$ ).<sup>2</sup> Figure 4a shows a Raman spectrum of a monolayer  $\text{Ti}_3\text{C}_2\text{T}_x$  film on a  $\text{Si}/\text{SiO}_2$  substrate, which shows two characteristic  $\text{Ti}_3\text{C}_2\text{T}_x$  peaks centered at

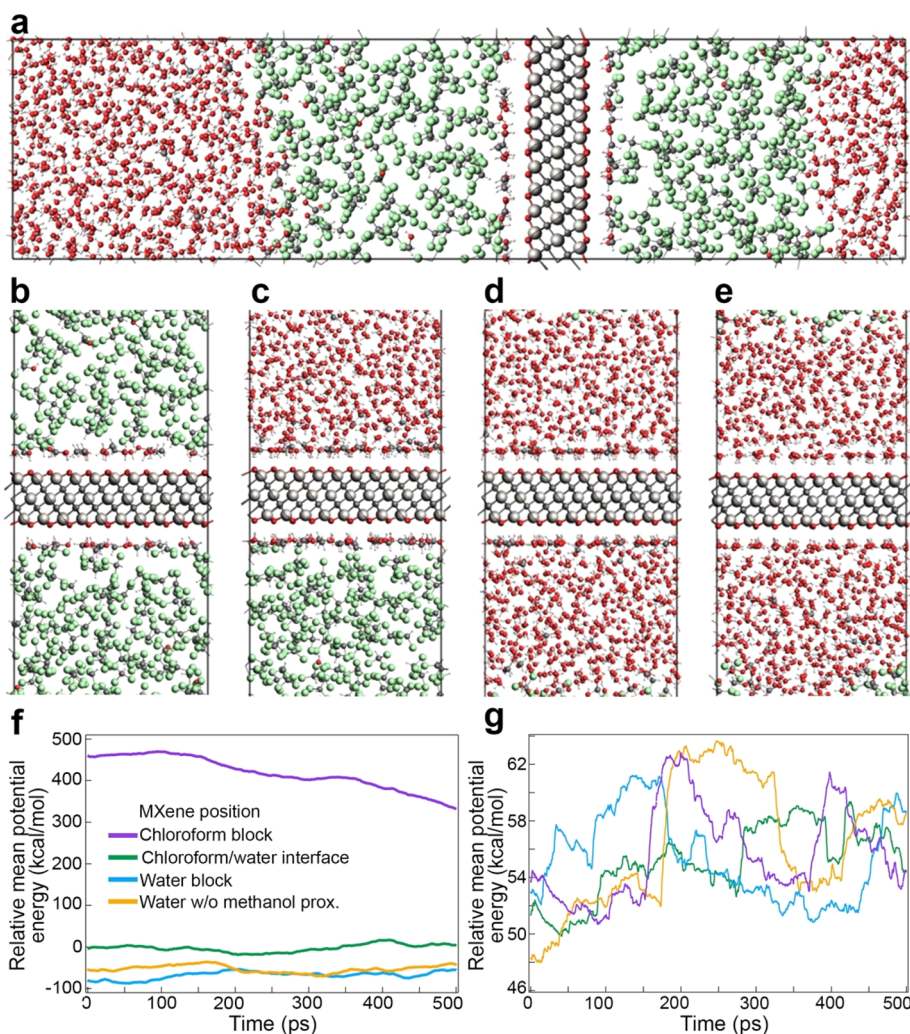


**Figure 5.** Snapshots showing different configurations after 500 ps of ReaxFF MD simulation and relative potential energy. (a) Representative full domain of the configurations simulated with chlorine atoms (green), carbon (dark gray), titanium (gray), oxygen (red), and hydrogen (white). (b–e) Close-up of the interface in the proximity of the MXene surface. From left to right: MXene solvated by chloroform, MXene at the liquid/liquid interface, MXene solvated by water, and MXene solvated by water with no preadsorption of methanol on its surface. (f,g) The relative running average of potential energy and its standard deviation for the configurations simulated.

$\sim 300\text{ cm}^{-1}$  and  $\sim 975\text{ cm}^{-1}$ . The strong peak at  $521\text{ cm}^{-1}$  corresponds to the Si substrate. Therefore, to provide some assessment of coverage, we obtained Raman spectra from a  $68.5 \times 44.5\ \mu\text{m}^2$  area and mapped the peak height intensity of the MXene peak at  $\sim 300\text{ cm}^{-1}$  to the Si peak (Figure 4b). While we cannot derive any thickness values based on these spectra, we find that MXene peaks are everywhere in the region, fluctuating in relative intensity by  $<25\%$ . Three spectra (1, 2, and 3) from three different areas (green, yellow, and orange) on the map in Figure 4b show the mean and extremities of our measurements. Next, to gain a deeper insight into the packing density and fractional area coverage of the films, we used AFM and SEM. Figure S8 shows SEM images of monolayer  $\text{Ti}_3\text{C}_2\text{T}_x$  films transferred onto the Si chips. The  $\text{SiN}_x$  membranes appear as dark areas beneath the  $\text{Ti}_3\text{C}_2\text{T}_x$  film because electrons are only weakly scattered from the ultrathin membrane. We used ImageJ software<sup>53</sup> to calculate the fractional area covered with monolayer  $\text{Ti}_3\text{C}_2\text{T}_x$  films based on finding the optimum threshold intensity that differentiates the substrate from the monolayer and quantifying the substrate area. In Figure 4c,d, we show AFM and SEM images of MXene monolayer films, respectively, along with corresponding post-

analysis images after thresholding, which were used in our coverage analysis. For the AFM measurements, we used a  $\text{SiN}_x$  substrate, whereas for SEM measurements, we used 50 nm-thick freestanding  $\text{SiN}_x$  membranes supported by a Si chip. For these images, we find MXene coverage values of 93% and 91%, respectively, with similar coverage values obtained in other areas we inspected (see Figures S9 and S10 for other images). We conclude that our lateral assembly method produces a mosaic structure of closely packed flakes that cover  $>90\%$  of the substrate following the transfer.

We conducted further analysis of the AFM images to calculate the fractional overlap/ridge areas (with more than one layer of MXene). Figure S11 shows four AFM images before (left) and after (right) analysis with void areas and overlap areas highlighted in red and blue, respectively. This analysis indicates that  $\sim 75\%$  of the MXene films are true monolayers, while the rest are either void or overlap. However, we note that the overlap area fractions are overestimated since they include a few occasional bilayer MXene flakes that form a part of the assembly (see yellow arrow in Figure S11).

To further understand the interactions of MXenes with their solvent environments, we have carried out reactive force-field

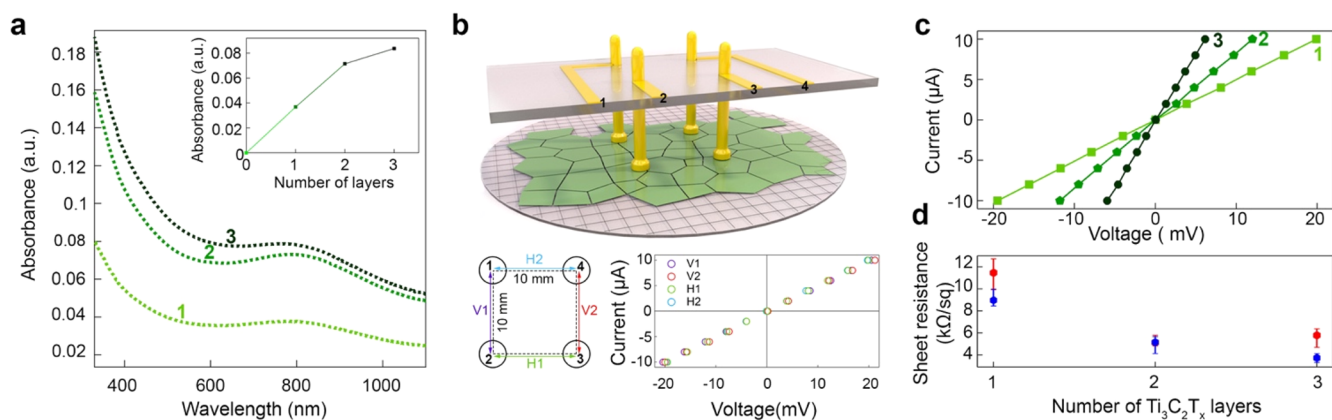


**Figure 6.** Optical and electrical characterization of monolayer and multilayer  $\text{Ti}_3\text{C}_2\text{T}_x$  films. (a) UV-vis absorbance spectra of monolayer, bilayer, and trilayer  $\text{Ti}_3\text{C}_2\text{T}_x$  films, corrected for substrate absorbance. Inset shows the absorbance of the films at 550 nm. (b) Schematic of vdP apparatus used for sheet resistance measurement of the films. Bottom: Top view of the apparatus showing the location of corresponding electrodes from 1 to 4 and edges of the square area where electrical measurements were carried out (H1, H2, V1, and V2). Corresponding  $I$ - $V$  curves of current sweep across each edge is shown on the right. (c) Representative  $I$ - $V$  curves of monolayer, bilayer, and trilayer  $\text{Ti}_3\text{C}_2\text{T}_x$  films. (d) Sheet resistance of  $\text{Ti}_3\text{C}_2\text{T}_x$  films vs the number of  $\text{Ti}_3\text{C}_2\text{T}_x$  layers. Markers show the average of the sheet resistance values and the lines show the range of the values for six measurements on six different areas on the sample.

(ReaxFF) MD simulations. From the NPT ensemble MD simulations of  $-\text{OH}$  group edge-terminated  $\text{Ti}_3\text{C}_2\text{O}_2$  MXene (see Figure S12 and Supplementary Movies S3–S5), we observe that methanol molecules diffuse toward the MXene, adsorbing on its surface. This enables the MXene to be stabilized also when solvated by chloroform, while the absence of methanol forces the chloroform-solvated MXene to diffuse toward the water region (*cf.* Figures S12 and S13). Simulations with an edge-free MXene spanning the  $xy$ -plane separating the ternary solvent were used to quantify the energetics of these interactions. To bypass the diffusive time scale of methanol transport to the surface, half of the methanol content was initialized on the MXene, and the remaining methanol was initialized at the water/chloroform interface. Figure 5a–e shows the four different configurations considered: MXene solvated by chloroform or water, MXene at the interface of water/chloroform, and MXene solvated by water with no preadsorbed methanol. The running average potential energy and standard deviation vs time for each system are shown in Figure 5f,g. Although methanol stabilizes the MXene chloroform interface (Figure 5a,b), its reduced hydrogen-bond formation capability to the MXene surface, compared with water, makes it energetically unfavorable when compared against MXene at the liquid/liquid interface or solvated by water. However, the distinction of a favorable configuration between the water-solvated, interfacial, and water-solvated without adsorbed methanol is not straightforward. While the mean potential energy of the water-solvated MXene (with and without adsorbed methanol) is lower in energy by  $\sim 60$  kcal/mol in comparison to MXene at the interface, the standard deviation in energies of a similar magnitude suggests a likelihood of all three configurations. Substantially longer MD simulations will be required to statistically separate the energies of these configurations, but our current simulations demonstrate that addition of methanol indeed makes the chloroform/water interface more accessible to the MXene flakes, thus connecting with the experiments. It must be noted that there is no additional methanol added to the solvent to compensate for the adsorption on the MXene in our simulations. Therefore, it is possible that upon further diffusion of methanol toward the surface, the difference between the

three configurations is reduced. Thus, these simulations suggest that the availability of methanol at the water/chloroform interface provides stability *via* hydrogen bonds within the chloroform region, allowing the liquid/liquid interface to be an equally favorable site for the MXene, enabling its film-like assembly.

So far, we have shown that the lateral self-assembly method is capable of producing ultrathin, uniform monolayer, and packed  $\text{Ti}_3\text{C}_2\text{T}_x$  films. To investigate the sequential assembly of bilayers and trilayers, we repeated our transfer method by lifting a monolayer film onto a substrate, drying the substrate, reimmersing the substrate in chloroform, repeating lateral self-assembly of MXene flakes at the interface, and emerging the substrate from the chloroform phase. Figure S14 shows AFM images of bilayer  $\text{Ti}_3\text{C}_2\text{T}_x$  films on a  $\text{SiN}_x$  substrate. The corresponding line height profiles of bilayer films are shown in Figure S14c,d, demonstrating the bilayer  $\text{Ti}_3\text{C}_2\text{T}_x$  thickness is measured around 4.5 nm with average surface roughness in the range of 2.6–3 nm. Height uniformity in these images confirms that the structure and integrity of each transferred layer are not adversely affected by a sequential transfer process. We examined the resulting multilayer films using optical spectroscopy and electrical conductivity measurements. Figure 6a shows the UV-vis absorbance spectra of monolayer, bilayer, and trilayer  $\text{Ti}_3\text{C}_2\text{T}_x$  films on a glass substrate. As seen in the spectra, absorbance increases with an increasing number of layers. The inset shows the absorbance for monolayer, bilayer, and trilayer films at 550 nm, showing that although the increase is not linear due to overlaps at the edges, it is in qualitative agreement with the previous studies.<sup>43</sup> Due to the inherent in-plane conductivity of  $\text{Ti}_3\text{C}_2\text{T}_x$  flakes, we examined how the number of MXene layers affects the electrical properties of the films. We used the van der Pauw method (vdP) to measure the sheet resistance of the films<sup>54</sup> using a homemade apparatus and a Keithley 2401 source meter (Tektronix, Inc., USA). Figure 6b shows the schematic of the apparatus, which consists of a square grid of four gold electrodes separated by 10 mm. Four wires connect to each electrode at points 1, 2, 3, and 4 and attach to the Keithley source meter (see Figure S15 for an image of the experimental setup). Figure 6b also shows a schematic top-view image of the

electrodes and depicts the four edges of the film, two horizontal (H1 and H2), and two vertical (V1 and V2), where conductivity measurements are carried out. First, the current is sourced along each edge (horizontal and vertical), and voltage is measured along the opposite edge. This is repeated for all combinations which result in four independent measurements. Current *vs* voltage (*I*–*V*) curves of these measurements for a monolayer  $\text{Ti}_3\text{C}_2\text{T}_x$  film transferred onto a glass substrate are shown in Figure 6b. Due to the uniformity of the film within this  $10 \times 10 \text{ mm}^2$  area, the four *I*–*V* curves are identical. Figure 6c shows one representative *I*–*V* curve for each monolayer, bilayer, and trilayer  $\text{Ti}_3\text{C}_2\text{T}_x$  films measured after the sequential transfer of each layer. From the resistance values obtained by *I*–*V* measurements, sheet resistance values can be calculated (see Materials and Methods section for details). Figure 6d shows the sheet resistance values for two samples of  $\text{Ti}_3\text{C}_2\text{T}_x$  films on a glass substrate with a thickness of 1, 2, and 3 layers. As expected, as the thickness of the film increases, the sheet resistance decreases. In general, our monolayer films show a higher sheet resistance (9–11  $\text{k}\Omega/\text{sq}$ ) compared to the recent study by Yun *et al.*,<sup>43</sup> which showed a resistance of 1.5  $\text{k}\Omega/\text{sq}$  for a monolayer film. We attribute this discrepancy to the mosaic morphology of our films, in which flake-to-flake contact is edge-to-edge with minimal overlapping. Despite the higher resistance, we find that our films exhibit an ohmic response and that resistance drops with increasing number of layers.

Finally, in Table S1, we have compared the advantages and disadvantages of the various methods of large-scale 2D materials film fabrication with single-layer precision such as spin coating, Langmuir–Blodgett, layer-by-layer assembly, and interfacial assembly. Compared to other methods, one advantage of our wafer-scale lateral self-assembly is the resulting uniform film structure across the entire film area, which is unlike the spin-coating method that results in a compact monolayer film only at the center of the substrate. Compared to the Langmuir transfer method, our assembly method is much faster (under 30 min for film formation on a 3 in. wafer) and, further, does not require any special apparatus apart from a PTFE dish. As discussed in our previous study,<sup>46</sup> the driving force for film formation at the liquid/liquid interface is a combination of repulsion force, capillary force, and surface tension, which results in a delicate organization of the resulting mosaic film structure. Therefore, our lateral assembly method results in smoother and more organized films than those produced by spontaneous absorption of flakes from solution, such as the layer-by-layer assembly method.

## CONCLUSION

In summary, we have shown here that lateral self-assembly of MXene films at a liquid/liquid interface produces uniform mosaic-type monolayers that span over large areas (we have coated up to 3 in. substrates). We have studied the film morphology of our coated substrates at various length scales using a combination of tools that include AFM, SEM, and TEM imaging as well as ellipsometric and Raman mapping. Moreover, the sequential transfer of single-layer films on a substrate enables the fabrication of multilayer films without peeling off the preceding layers. This was confirmed by the change in sheet resistance and optical properties of the films upon sequential deposition of multilayer films. MD simulation results showed the presence of methanol at the water/

chloroform interface renders the interface a favorable site for MXene flakes to reside and self-assemble.

Use of 2D material devices for biosensing has been of particular interest in recent years because of their large surface area to volume ratios and their unique optical and electrical properties. Recent demonstrations of CRISPR-enhanced graphene-based field-effect transistors,<sup>55</sup> MXene-based neuro-electronic devices,<sup>56</sup> graphene/MoS<sub>2</sub> heterostructure-based sensors for DNA hybridization,<sup>57</sup> and 2D material-based nanoscale devices for biomolecule probing<sup>58</sup> are just a few examples of 2D material-based biosensors. A particular hurdle that limits the adoption of these devices as biosensors is the difficult step of transferring the 2D materials onto their perspective substrate in a guaranteed high yield and with appropriate alignment. In 2D material-based nanopore sensing devices, small-scale device fabrication is complicated by a lack of straightforward methods for wafer-scale fabrication and/or transfer methods.<sup>59</sup> As we have shown in our previous study,<sup>46</sup> this is also an existing issue for MXenes. Our straightforward method for large-area monolayer to multilayer MXene films could lead to highly functioning MXene-based biosensing devices.

Finally, while we have focused here on large-scale self-assembly of  $\text{Ti}_3\text{C}_2\text{T}_x$  flakes, our method should be compatible with a variety of other members of the MXene family. Considering the 30+ different MXene compositions experimentally synthesized so far, our method offers an attractive approach for producing large-area uniform films that may find use in applications that require hydrophilic and electrically conductive films with tunable optical properties such as transparent conductive electrodes for bioelectronics, illuminated displays, and other applications.

## MATERIALS AND METHODS

**MXenes Synthesis.**  $\text{Ti}_3\text{C}_2\text{T}_x$  MXene flakes with large lateral sizes were synthesized according to previous reports in the literature.<sup>49</sup> Initially, for every 1 g of the MAX phase, the mixed salt-acid etching solution was prepared by adding 1 g of LiF powder (98.5%, Alfa Aesar) to 20 mL of 6 M HCl solution (ACS grade, BDH), followed by stirring for 15 min to completely dissolve the LiF powder in the acid solution. The etching process was started by slowly adding 1 g of MAX phase powder ( $\text{Ti}_3\text{AlC}_2$  synthesized according to previous work)<sup>60</sup> to the etching solution. The etching container was placed into an ice bath during the addition of the MAX phase to avoid excessive heat generation due to the exothermic nature of the reaction. The etching solution was stirred at 550 rpm (by using a PTFE-coated magnetic bar) continually for 24 h at 35 °C. After 24 h, the solution containing etched MXene multilayers was divided into four different centrifuge vials, and 45 mL of DI water was added to them to start the washing process. The solutions were then shaken by hand for 1 min and centrifuged at 3500 rpm (Eppendorf 5810R) for 3 min, after which the supernatant was poured out. The washing process was continued several times, each time adding 45 mL of DI water, followed by manual shaking of the solutions for 2 min, and then centrifuging them at 3,500 rpm for 3 min until a dark green supernatant was observed (pH > 4.5). The supernatant after this stage is called the delaminated  $\text{Ti}_3\text{C}_2\text{T}_x$  dispersion. The initial delaminated solution (the first supernatant after the washing step was complete) was poured out, and DI water was added to the sediments. The solutions were shaken for another 2 min, and this time centrifuged at 3,500 rpm for 1 h to collect the large flake size MXene solutions (pH ~ 5).

**Wafer-Scale Lateral Self-Assembly of  $\text{Ti}_3\text{C}_2\text{T}_x$  MXene and Transfer on Substrate.** Monolayer MXene film formation was carried out by optimizing our previously reported lateral interfacial self-assembly method.<sup>46</sup> MXene dispersion was first diluted to the

desired concentration and then mixed with methanol to a 1:8 volume ratio. The substrate of desire was submerged in a chloroform bath, and the dispersion was added to the chloroform until the droplet size enlarged to the size of the substrate. After flakes were self-assembled on the droplet/chloroform interface, excess chloroform was removed from the bath and the film level lowered down to reach the substrate. Afterward, the substrate was lifted and baked at 100 °C for ~30 min to dry. The substrates were kept in a vacuum desiccator until use. We note that the concentration of the dispersion plays an important role in the final morphology of the film. Due to flake size heterogeneity, we prefer to use UV-vis absorbance to quantify MXene concentration. The film concentration according to the spectrum shown in Figure 1 produces a well-packed monolayer film structure. However, further optimization of the dispersion after the characterization of the initial film is sometimes required to achieve the desired morphology.

**Imaging Techniques.** For SEM and TEM imaging, monolayer  $\text{Ti}_3\text{C}_2\text{T}_x$  films were transferred onto Si chips with fabricated  $50 \times 50 \mu\text{m}^2$  50 nm-thick  $\text{SiN}_x$  membranes at their center. For AFM imaging, a film was transferred onto  $\text{SiN}_x$  substrates. High-resolution TEM imaging was done using a JEOL 2010FEG operating in bright-field mode at 200 kV. SEM was done using JSM-IT200 at 3.0 kV accelerating voltage. AFM measurements were carried out by the FastScan AFM instrument (Bruker Instruments, Billerica, MA) using ScanAsyst cantilevers (Bruker Instruments) performing at the FastScan device's ScanAsyst Mode. The roughness average ( $R_a$ ) parameter in the Roughness tool in Gwyddion software was used to report the average surface roughness values.

**Ellipsometry Spectroscopy and Mapping.** Ellipsometry measurements were carried out using HORIBA UVISSEL 2 Ellipsometer (HORIBA Scientific, USA) on monolayer  $\text{Ti}_3\text{C}_2\text{T}_x$  films deposited on Si substrate. Real ( $n$ ) and imaginary ( $k$ ) refractive indices previously developed<sup>38,51</sup> were used to make a reference file for  $\text{Ti}_3\text{C}_2\text{T}_x$  using DeltaPsi2 software. Using reference files for modeling, the optical constants are fixed for fitting, and only the thickness changes. We produced the model using DeltaPsi2 software based on the layered structure, consisting of Si,  $\text{SiO}_2$  (due to the presence of native oxide on the Si surface), and  $\text{Ti}_3\text{C}_2\text{T}_x$  layers (Figure S4). Figure S4 shows how well our model fits the measured  $\Psi$  and  $\Delta$  values obtained from a monolayer  $\text{Ti}_3\text{C}_2\text{T}_x$  film at two points on the wafer. For ellipsometry mapping, the DeltaPsi2 software mapping recipe feature was used to design an automated 81-point measurement at a wavelength range of 300–800 nm with a 70° incidence angle on a predesigned circular grid with a 40 mm diameter. The measurement results ( $\Psi$  and  $\Delta$  values) at each point were fitted to the layered model consisting of Si/ $\text{SiO}_2$ / $\text{Ti}_3\text{C}_2\text{T}_x$  to calculate the thickness. Using X, Y coordinates of grid points and thickness values, the Voronoi interpolation method was adopted, using Igor Pro software, to map the measurement results to the whole wafer area. For the effective medium approximation (EMA) model, we used the Bruggeman EMA method in DeltaPsi2 software to fit the model to our experimental data. The layered model consists of a Si layer, a  $\text{SiO}_2$  layer, and a layer with a mixture of  $\text{Ti}_3\text{C}_2\text{T}_x$  and void (Figure S6, inset). The resulting fitting parameters, percentage of void and MXene film (coverage), and the thickness of the MXene film at each point were used for interpretation of the model.

**Raman Spectroscopy and Mapping.** The Raman measurements were carried out using a Thermo Scientific DXR2xi Raman Imaging Microscope on monolayer  $\text{Ti}_3\text{C}_2\text{T}_x$  films deposited on 300 nm-thick  $\text{SiO}_2$  substrate. The excitation source was a 455 nm laser with 0.5  $\mu\text{m}$  spot size. The laser power was kept at 2 mW with a 1 s exposure time for 10 scans per position. Mapping was done on a  $68.5 \times 44.5 \mu\text{m}^2$  area using OminiCX Software.

**UV-vis Absorbance Measurement.** UV-vis absorbance measurements were carried out using a PerkinElmer Lambda 35 UV-vis-NIR spectrophotometer on monolayer, bilayer, and trilayer  $\text{Ti}_3\text{C}_2\text{T}_x$  films deposited on glass substrates in the range of 330–1100 nm. The effect of the glass substrates was removed by placing an identical clean glass slide in the reference beam position of the spectrophotometer, and hence, the absorbance spectra (shown in

Figure 6a) are representative for the  $\text{Ti}_3\text{C}_2\text{T}_x$  films without any contribution from the substrate.

**Conductivity Measurement.** The conductivity measurements were carried out using Keithley 2401 source meter and a homemade apparatus on monolayer, bilayer, and trilayer  $\text{Ti}_3\text{C}_2\text{T}_x$  films deposited on glass substrates. The apparatus consists of four gold electrodes located at four corners of a square with a 10 mm length (shown in Figure 6b,c). To calculate sheet resistance, two sets of measurements were carried out. The first set is to measure the voltage drop across each horizontal line of the square (H1 or H2) by the sourcing current across the opposite edge, followed by calculating the resistance from the slope of the  $I$ - $V$  curves ( $R_{\text{H1}}$ ,  $R_{\text{H2}}$ ). The second set is to measure the voltage drop across each vertical line of the square (V1 or V2) by sourcing current across the opposite edge ( $R_{\text{V1}}$ ,  $R_{\text{V2}}$ ). After the four measurement sweeps were taken, the sheet resistance was calculated as follows:

$$R_{\text{horizontal}} = \frac{R_{\text{H1}} + R_{\text{H2}}}{2}$$

$$R_{\text{vertical}} = \frac{R_{\text{V1}} + R_{\text{V2}}}{2}$$

$$e^{-\pi R_{\text{horizontal}}/R_s} + e^{-\pi R_{\text{vertical}}/R_s} = 1, \quad R_s = \text{sheet resistance}$$

**MD Simulations.** All MD simulations using the ReaxFF potential<sup>61,62</sup> were carried out using the AMS suite distributed by SCM (see [www.scm.com](http://www.scm.com)). To enable interactions with chloroform, Cl/C/H/O parameters were added to the force field developed for  $\text{Ti}_3\text{C}_2$  MXenes<sup>63,64</sup> with corrections to the Ti/O/H parameters to improve the ReaxFF description of surface defects and de/protonation kinetics.<sup>65</sup> The force field and details on the parametrization can be found in the SI and Table S2. A  $21.56 \times 26.67 \text{ \AA}^2$  slab of MXene was equilibrated in bulk water under NVT ensemble MD simulation at 500 K to form terminating -OH groups, and any adsorbed water molecules were removed. The solvents, chloroform and methanol and water (1:8 volume ratio), were initialized in a periodic domain of size  $43.15 \times 46.47 \times 16.87 \text{ \AA}^3$  each, and the edge-terminated MXene was placed at various positions between the solvents, that is, at the interface of water and chloroform, or in either solvent. The dynamics was studied under an NPT ensemble ( $P = 1$  atm,  $T = 300$  K) simulation for 1 ns using the Berendsen barostat and thermostat (5000 and 100 fs damping coefficients, respectively). To quantify the energetics of MXene at different positions, an edge-free orthogonalized MXene spanning the  $xy$ -plane of size  $26.25 \times 30.30 \text{ \AA}^2$  was considered separating the solvent, each solvent with  $z$ -axis length of 40  $\text{ \AA}$ . These simulations were first equilibrated using the NPT-ensemble for 100 ps to prevent artifacts due to initialization, followed by NVT ensemble MD simulations for 500 ps for data collection. The running average and standard deviation of potential energy were calculated using a sampling window of 150 ps.

## ASSOCIATED CONTENT

### Supporting Information

The Supporting Information is available free of charge at <https://pubs.acs.org/doi/10.1021/acsnano.0c06393>.

AFM/SEM/TEM images of the monolayer MXene film, refractive indices of  $\text{Ti}_3\text{C}_2\text{T}_x$  film, ellipsometric modeling and goodness-of-fit, ellipsometry effective medium approximation model analysis, analyzed AFM and SEM images showing substrate coverage, final snapshots of a  $\text{Ti}_3\text{C}_2\text{T}_x$  flake in the solvent after 1.5 ns of simulation, snapshot of a  $\text{Ti}_3\text{C}_2\text{T}_x$  flake in chloroform during early stages and after 1.5 ns, AFM images of the bilayer MXene film, vdP experimental setup, comparison between methods of large-scale film fabrication of 2D materials, comparison of ReaxFF and DFT values for molecular chloroform and chloroform crystal (PDF)

Movie S1: Detailed steps of  $\text{Ti}_3\text{C}_2\text{T}_x$  film assembly and transfer (MP4)

Movie S2: MXene flake rearrangement after mechanical disruption of the self-assembled film (MP4)

Movie S3: MD simulation of  $\text{Ti}_3\text{C}_2\text{T}_x$  flake at the liquid/liquid interface of the ternary mixture (MP4)

Movie S4: MD simulation of  $\text{Ti}_3\text{C}_2\text{T}_x$  flake solvated by water in ternary mixture (MP4)

Movie S5: MD simulation of  $\text{Ti}_3\text{C}_2\text{T}_x$  flake solvated by chloroform in ternary mixture (MP4)

## AUTHOR INFORMATION

### Corresponding Author

**Meni Wanunu** – Department of Physics and Department of Chemistry and Chemical Biology, Northeastern University, Boston, Massachusetts 02115, United States; [orcid.org/0000-0002-9837-0004](https://orcid.org/0000-0002-9837-0004); Email: [wanunu@neu.edu](mailto:wanunu@neu.edu)

### Authors

**Mehrnaz Mojtabavi** – Department of Bioengineering, Northeastern University, Boston, Massachusetts 02115, United States

**Armin VahidMohammadi** – Innovation Partnership Building, UConn TechPark, University of Connecticut, Storrs, Connecticut 06269, United States; [orcid.org/0000-0002-6284-7560](https://orcid.org/0000-0002-6284-7560)

**Karthik Ganeshan** – Department of Mechanical Engineering, Pennsylvania State University, University Park, Pennsylvania 16802, United States; [orcid.org/0000-0002-3911-4246](https://orcid.org/0000-0002-3911-4246)

**Davoud Hejazi** – Department of Physics, Northeastern University, Boston, Massachusetts 02115, United States; [orcid.org/0000-0002-5215-6395](https://orcid.org/0000-0002-5215-6395)

**Sina Shahbazmohammadi** – Innovation Partnership Building, UConn TechPark, University of Connecticut, Storrs, Connecticut 06269, United States

**Swastik Kar** – Department of Physics, Northeastern University, Boston, Massachusetts 02115, United States

**Adri C. T. van Duin** – Department of Mechanical Engineering, Pennsylvania State University, University Park, Pennsylvania 16802, United States; [orcid.org/0000-0002-3478-4945](https://orcid.org/0000-0002-3478-4945)

Complete contact information is available at: <https://pubs.acs.org/10.1021/acsnano.0c06393>

### Notes

The authors declare no competing financial interest.

## ACKNOWLEDGMENTS

We acknowledge the National Science Foundation (DMR 1710211) for funding this work. The authors thank Kathleen Maleski, Yury Gogotsi, and Aaron Fafarman for providing us with the values for modeling the ellipsometric measurements. The authors acknowledge Tzahi Cohen-Karni and Raghav Garg (Carnegie-Mellon University) for loaning us the vdP apparatus and providing a protocol. The authors thank Joshua Gallaway and Matthew Kim for use of their Raman spectroscopy and mapping tool. We thank David Hoogerheide for providing us with the 3 in. Si wafer for ellipsometric measurements. K.G. and A.C.T.v.D. performed the ReaxFF MD simulations and acknowledge funding from the Fluid Interface Reactions, Structures and Transport (FIRST), an Energy Frontier Research Center funded by the US Depart-

ment of Energy, Office of Science, Office of Basic Energy Sciences.

## REFERENCES

- (1) Bhimanapati, G. R.; Lin, Z.; Meunier, V.; Jung, Y.; Cha, J.; Das, S.; Xiao, D.; Son, Y.; Strano, M. S.; Cooper, V. R.; Liang, L.; Louie, S. G.; Ringe, E.; Zhou, W.; Kim, S. S.; Naik, R. R.; Sumpter, B. G.; Terrones, H.; Xia, F.; Wang, Y.; et al. Recent Advances in Two-Dimensional Materials beyond Graphene. *ACS Nano* **2015**, *9*, 11509–11539.
- (2) Anasori, B.; Lukatskaya, M. R.; Gogotsi, Y. 2D Metal Carbides and Nitrides (Mxenes) for Energy Storage. *Nat. Rev. Mater.* **2017**, *2*, 16098.
- (3) Zeng, M.; Xiao, Y.; Liu, J.; Yang, K.; Fu, L. Exploring Two-Dimensional Materials toward the Next-Generation Circuits: From Monomer Design to Assembly Control. *Chem. Rev.* **2018**, *118*, 6236–6296.
- (4) Donarelli, M.; Ottaviano, L. 2D Materials for Gas Sensing Applications: A Review on Graphene Oxide, MoS<sub>2</sub>, WS<sub>2</sub> and Phosphorene. *Sensors* **2018**, *18*, 3638.
- (5) Danda, G.; Drndić, M. Two-Dimensional Nanopores and Nanoporous Membranes for Ion and Molecule Transport. *Curr. Opin. Biotechnol.* **2019**, *55*, 124–133.
- (6) Meng, Z.; Stolz, R. M.; Mendecki, L.; Mírca, K. A. Electrically-Transduced Chemical Sensors Based on Two-Dimensional Nanomaterials. *Chem. Rev.* **2019**, *119*, 478–598.
- (7) Bolotsky, A.; Butler, D.; Dong, C.; Gerace, K.; Glavin, N. R.; Muratore, C.; Robinson, J. A.; Ebrahimi, A. Two-Dimensional Materials in Biosensing and Healthcare: From *in Vitro* Diagnostics to Optogenetics and Beyond. *ACS Nano* **2019**, *13*, 9781–9810.
- (8) Dervin, S.; Dionysiou, D. D.; Pillai, S. C. 2D Nanostructures for Water Purification: Graphene and Beyond. *Nanoscale* **2016**, *8*, 15115–15131.
- (9) Rasool, K.; Pandey, R. P.; Rasheed, P. A.; Buczek, S.; Gogotsi, Y.; Mahmoud, K. A. Water Treatment and Environmental Remediation Applications of Two-Dimensional Metal Carbides (Mxenes). *Mater. Today* **2019**, *30*, 80–102.
- (10) Pomerantseva, E.; Bonaccorso, F.; Feng, X.; Cui, Y.; Gogotsi, Y. Energy Storage: The Future Enabled by Nanomaterials. *Science* **2019**, *366*, No. eaan8285.
- (11) Macha, M.; Marion, S.; Nandigana, V. V. R.; Radenovic, A. 2D Materials as an Emerging Platform for Nanopore-Based Power Generation. *Nature Reviews Materials*. **2019**, *4*, 588–605.
- (12) Ariga, K.; Yamauchi, Y.; Mori, T.; Hill, J. P. 25th Anniversary Article: What Can Be Done with the Langmuir-Blodgett Method? Recent Developments and Its Critical Role in Materials Science. *Adv. Mater.* **2013**, *25*, 6477–6512.
- (13) Shao, J.-J.; Lv, W.; Yang, Q.-H. Self-Assembly of Graphene Oxide at Interfaces. *Adv. Mater.* **2014**, *26*, 5586–5612.
- (14) Ning, J.; Wang, D.; Chai, Y.; Feng, X.; Mu, M.; Guo, L.; Zhang, J.; Hao, Y. Review on Mechanism of Directly Fabricating Wafer-Scale Graphene on Dielectric Substrates by Chemical Vapor Deposition. *Nanotechnology* **2017**, *28*, 284001.
- (15) Zavabeti, A.; Jannat, A.; Zhong, L.; Haidry, A. A.; Yao, Z.; Ou, J. Z. Two-Dimensional Materials in Large-Areas: Synthesis, Properties and Applications. *Nano-Micro Lett.* **2020**, *12*, 66.
- (16) Cote, L. J.; Kim, F.; Huang, J. Langmuir-Blodgett Assembly of Graphite Oxide Single Layers. *J. Am. Chem. Soc.* **2009**, *131*, 1043–1049.
- (17) Kim, F.; Cote, L. J.; Huang, J. Graphene Oxide: Surface Activity and Two-Dimensional Assembly. *Adv. Mater.* **2010**, *22*, 1954–1958.
- (18) Zheng, Q.; Ip, W. H.; Lin, X.; Yousefi, N.; Yeung, K. K.; Li, Z.; Kim, J.-K. Transparent Conductive Films Consisting of Ultralarge Graphene Sheets Produced by Langmuir-Blodgett Assembly. *ACS Nano* **2011**, *5*, 6039–6051.
- (19) Kim, J. W.; Kang, D.; Kim, T. H.; Lee, S. G.; Byun, N.; Lee, D. W.; Seo, B. H.; Ruoff, R. S.; Shin, H. S. Mosaic-Like Monolayer of Graphene Oxide Sheets Decorated with Tetrabutylammonium Ions. *ACS Nano* **2013**, *7*, 8082–8088.

- (20) Lin, X.; Jia, J.; Yousefi, N.; Shen, X.; Kim, J.-K. Excellent Optoelectrical Properties of Graphene Oxide Thin Films Deposited on a Flexible Substrate by Langmuir-Blodgett Assembly. *J. Mater. Chem. C* **2013**, *1*, 6869–6877.
- (21) Hidalgo, R. S.; López-Díaz, D.; Velázquez, M. M. Graphene Oxide Thin Films: Influence of Chemical Structure and Deposition Methodology. *Langmuir* **2015**, *31*, 2697–2705.
- (22) Yamaguchi, H.; Eda, G.; Mattevi, C.; Kim, H.; Chhowalla, M. Highly Uniform 300 mm Wafer-Scale Deposition of Single and Multilayered Chemically Derived Graphene Thin Films. *ACS Nano* **2010**, *4*, 524–528.
- (23) Matsuba, K.; Wang, C.; Saruwatari, K.; Uesusuki, Y.; Akatsuka, K.; Osada, M.; Ebina, Y.; Ma, R.; Sasaki, T. Neat Monolayer Tiling of Molecularly Thin Two-Dimensional Materials in 1 min. *Science Advances* **2017**, *3*, No. e1700414.
- (24) Shen, J.; Hu, Y.; Li, C.; Qin, C.; Shi, M.; Ye, M. Layer-by-Layer Self-Assembly of Graphene Nanoplatelets. *Langmuir* **2009**, *25*, 6122–6128.
- (25) Lee, D. W.; Hong, T.-K.; Kang, D.; Lee, J.; Heo, M.; Kim, J. Y.; Kim, B.-S.; Shin, H. S. Highly Controllable Transparent and Conducting Thin Films Using Layer-by-Layer Assembly of Oppositely Charged Reduced Graphene Oxides. *J. Mater. Chem.* **2011**, *21*, 3438–3442.
- (26) Li, X.; Zhang, G.; Bai, X.; Sun, X.; Wang, X.; Wang, E.; Dai, H. Highly Conducting Graphene Sheets and Langmuir-Blodgett Films. *Nat. Nanotechnol.* **2008**, *3*, 538–542.
- (27) Biswas, S.; Drzal, L. T. A Novel Approach to Create a Highly Ordered Monolayer Film of Graphene Nanosheets at the Liquid-Liquid Interface. *Nano Lett.* **2009**, *9*, 167–172.
- (28) Yun, T.; Kim, J.-S.; Shim, J.; Choi, D. S.; Lee, K. E.; Koo, S. H.; Kim, I.; Jung, H. J.; Yoo, H.-W.; Jung, H.-T.; Kim, S. O. Ultrafast Interfacial Self-Assembly of 2D Transition Metal Dichalcogenides Monolayer Films and Their Vertical and In-Plane Heterostructures. *ACS Appl. Mater. Interfaces* **2017**, *9*, 1021–1028.
- (29) Kim, K. S.; Zhao, Y.; Jang, H.; Lee, S. Y.; Kim, J. M.; Kim, K. S.; Ahn, J.-H.; Kim, P.; Choi, J.-Y.; Hong, B. H. Large-Scale Pattern Growth of Graphene Films for Stretchable Transparent Electrodes. *Nature* **2009**, *457*, 706–710.
- (30) Li, X.; Cai, W.; An, J.; Kim, S.; Nah, J.; Yang, D.; Piner, R.; Velamakanni, A.; Jung, I.; Tutuc, E.; Banerjee, S. K.; Colombo, L.; Ruoff, R. S. Large-Area Synthesis of High-Quality and Uniform Graphene Films on Copper Foils. *Science* **2009**, *324*, 1312–1314.
- (31) Hofrichter, J.; Szafrank, B. N.; Otto, M.; Echtermeyer, T. J.; Baus, M.; Majerus, A.; Geringer, V.; Ramsteiner, M.; Kurz, H. Synthesis of Graphene on Silicon Dioxide by a Solid Carbon Source. *Nano Lett.* **2010**, *10*, 36–42.
- (32) Kang, K.; Xie, S.; Huang, L.; Han, Y.; Huang, P. Y.; Mak, K. F.; Kim, C.-J.; Muller, D.; Park, J. High-Mobility Three-Atom-Thick Semiconducting Films with Wafer-Scale Homogeneity. *Nature* **2015**, *520*, 656–660.
- (33) Yu, H.; Liao, M.; Zhao, W.; Liu, G.; Zhou, X. J.; Wei, Z.; Xu, X.; Liu, K.; Hu, Z.; Deng, K.; Zhou, S.; Shi, J.-A.; Gu, L.; Shen, C.; Zhang, T.; Du, L.; Xie, L.; Zhu, J.; Chen, W.; Yang, R.; et al. Wafer-Scale Growth and Transfer of Highly-Oriented Monolayer MoS<sub>2</sub> Continuous Films. *ACS Nano* **2017**, *11*, 12001–12007.
- (34) Zhang, S.; Xu, H.; Liao, F.; Sun, Y.; Ba, K.; Sun, Z.; Qiu, Z.-J.; Xu, Z.; Zhu, H.; Chen, L.; Sun, Q.; Zhou, P.; Bao, W.; Zhang, D. W. Wafer-Scale Transferred Multilayer MoS<sub>2</sub> for High Performance Field Effect Transistors. *Nanotechnology* **2019**, *30*, 174002.
- (35) Li, S.; Lin, Y.-C.; Liu, X.-Y.; Hu, Z.; Wu, J.; Nakajima, H.; Liu, S.; Okazaki, T.; Chen, W.; Minari, T.; Sakuma, Y.; Tsukagoshi, K.; Suenaga, K.; Taniguchi, T.; Osada, M. Wafer-Scale and Deterministic Patterned Growth of Monolayer MoS<sub>2</sub> via Vapor-Liquid-Solid Method. *Nanoscale* **2019**, *11*, 16122–16129.
- (36) Naguib, M.; Mochalin, V. N.; Barsoum, M. W.; Gogotsi, Y. 25th Anniversary Article: Mxenes: A New Family of Two-Dimensional Materials. *Adv. Mater.* **2014**, *26*, 992–1005.
- (37) Tian, W.; VahidMohammadi, A.; Wang, Z.; Ouyang, L.; Beidaghi, M.; Hamed, M. M. Layer-by-Layer Self-Assembly of Pillared Two-Dimensional Multilayers. *Nat. Commun.* **2019**, *10*, 2558.
- (38) Dillon, A. D.; Ghidui, M. J.; Krick, A. L.; Griggs, J.; May, S. J.; Gogotsi, Y.; Barsoum, M. W.; Fafarman, A. T. Highly Conductive Optical Quality Solution-Processed Films of 2D Titanium Carbide. *Adv. Funct. Mater.* **2016**, *26*, 4162–4168.
- (39) Peng, Y.-Y.; Akuzum, B.; Kurra, N.; Zhao, M.-Q.; Alhabeab, M.; Anasori, B.; Kumbur, E. C.; Alshareef, H. N.; Ger, M.-D.; Gogotsi, Y. All-Mxene (2D Titanium Carbide) Solid-State Microsupercapacitors for On-Chip Energy Storage. *Energy Environ. Sci.* **2016**, *9*, 2847–2854.
- (40) Sarycheva, A.; Polemi, A.; Liu, Y.; Dandekar, K.; Anasori, B.; Gogotsi, Y. 2D Titanium Carbide (Mxene) for Wireless Communication. *Science Advances* **2018**, *4*, No. eaau0920.
- (41) Salles, P.; Quain, E.; Kurra, N.; Sarycheva, A.; Gogotsi, Y. Automated Scalpel Patterning of Solution Processed Thin Films for Fabrication of Transparent Mxene Microsupercapacitors. *Small* **2018**, *14*, 1802864.
- (42) Kim, S. J.; Choi, J.; Maleski, K.; Hantanasirisakul, K.; Jung, H.-T.; Gogotsi, Y.; Ahn, C. W. Interfacial Assembly of Ultrathin, Functional Mxene Films. *ACS Appl. Mater. Interfaces* **2019**, *11*, 32320–32327.
- (43) Yun, T.; Kim, H.; Iqbal, A.; Cho, Y. S.; Lee, G. S.; Kim, M.-K.; Kim, S. J.; Kim, D.; Gogotsi, Y.; Kim, S. O.; Koo, C. M. Electromagnetic Shielding of Monolayer Mxene Assemblies. *Adv. Mater.* **2020**, *32*, 1906769.
- (44) Petukhov, D. I.; Chumakov, A. P.; Kan, A. S.; Lebedev, V. A.; Eliseev, A. A.; Kononov, O. V.; Eliseev, A. A. Spontaneous Mxene Monolayer Assembly at the Liquid-Air Interface. *Nanoscale* **2019**, *11*, 9980–9986.
- (45) Kim, H.; Kee, J.; Seo, D.-R.; Lee, Y.; Ahn, C. W.; Koo, J. Large-Area 2D-Mxene Nanosheet Assemblies Using Langmuir-Schaefer Technique: Wrinkle Formation. *ACS Appl. Mater. Interfaces* **2020**, *12*, 42294–42301.
- (46) Mojtavavi, M.; VahidMohammadi, A.; Liang, W.; Beidaghi, M.; Wanunu, M. Single-Molecule Sensing Using Nanopores in Two-Dimensional Transition Metal Carbide (Mxene) Membranes. *ACS Nano* **2019**, *13*, 3042–3053.
- (47) Alhabeab, M.; Maleski, K.; Anasori, B.; Lelyukh, P.; Clark, L.; Sin, S.; Gogotsi, Y. Guidelines for Synthesis and Processing of Two-Dimensional Titanium Carbide (Ti<sub>3</sub>C<sub>2</sub>T<sub>x</sub> Mxene). *Chem. Mater.* **2017**, *29*, 7633–7644.
- (48) Li, Y.; Huang, S.; Wei, C.; Wu, C.; Mochalin, V. N. Adhesion of Two-Dimensional Titanium Carbides (Mxenes) and Graphene to Silicon. *Nat. Commun.* **2019**, *10*, 3014.
- (49) Lipatov, A.; Alhabeab, M.; Lukatskaya, M. R.; Boson, A.; Gogotsi, Y.; Sinitiskii, A. Effect of Synthesis on Quality, Electronic Properties and Environmental Stability of Individual Monolayer Ti<sub>3</sub>C<sub>2</sub>Mxene Flakes. *Advanced Electronic Materials* **2016**, *2*, 1600255.
- (50) Lipatov, A.; Lu, H.; Alhabeab, M.; Anasori, B.; Gruverman, A.; Gogotsi, Y.; Sinitiskii, A. Elastic Properties of 2D Ti<sub>3</sub>C<sub>2</sub>T<sub>x</sub> Mxene Monolayers and Bilayers. *Science Advances* **2018**, *4*, No. eaat0491.
- (51) Maleski, K.; Shuck, C. E.; Fafarman, A. T.; Gogotsi, Y. The Broad Chromatic Range of Two-Dimensional Transition Metal Carbides. *Adv. Opt. Mater.* **2020**, 2001563.
- (52) Sarycheva, A.; Gogotsi, Y. Raman Spectroscopy Analysis of the Structure and Surface Chemistry of Ti<sub>3</sub>C<sub>2</sub>T<sub>x</sub> Mxene. *Chem. Mater.* **2020**, *32*, 3480–3488.
- (53) Schneider, C. A.; Rasband, W. S.; Eliceiri, K. W. NIH Image to ImageJ: 25 Years of Image Analysis. *Nat. Methods* **2012**, *9*, 671–675.
- (54) Pauw, L. J. v. d. A Method of Measuring Specific Resistivity and Hall Effect of Discs of Arbitrary Shape. *Semiconductor Devices: Pioneering Papers*; World Scientific: Singapore, 1991; pp 174–182.
- (55) Hajian, R.; Balderston, S.; Tran, T.; deBoer, T.; Etienne, J.; Sandhu, M.; Wauford, N. A.; Chung, J.-Y.; Nokes, J.; Athaiya, M.; Paredes, J.; Peytavi, R.; Goldsmith, B.; Murthy, N.; Conboy, I. M.; Aran, K. Detection of Unamplified Target Genes via Crispr-Cas9 Immobilized on a Graphene Field-Effect Transistor. *Nature Biomedical Engineering* **2019**, *3*, 427–437.

(56) Driscoll, N.; Richardson, A. G.; Maleski, K.; Anasori, B.; Adewole, O.; Lelyukh, P.; Escobedo, L.; Cullen, D. K.; Lucas, T. H.; Gogotsi, Y.; Vitale, F. Two-Dimensional Ti<sub>3</sub>C<sub>2</sub>Mxene for High-Resolution Neural Interfaces. *ACS Nano* **2018**, *12*, 10419–10429.

(57) Loan, P. T. K.; Zhang, W.; Lin, C.-T.; Wei, K.-H.; Li, L.-J.; Chen, C.-H. Graphene/MoS<sub>2</sub> Heterostructures for Ultrasensitive Detection of DNA Hybridisation. *Adv. Mater.* **2014**, *26*, 4838–4844.

(58) Arjmandi-Tash, H.; Belyaeva, L. A.; Schneider, G. F. Single Molecule Detection with Graphene and Other Two-Dimensional Materials: Nanopores and Beyond. *Chem. Soc. Rev.* **2016**, *45*, 476–493.

(59) Thakur, M.; Macha, M.; Chernev, A.; Graf, M.; Lihter, M.; Deen, J.; Tripathi, M.; Kis, A.; Radenovic, A. Wafer-Scale Fabrication of Nanopore Devices for Single-Molecule DNA Biosensing Using MoS<sub>2</sub>. *Small Methods*. **2020**, *4*, 2000072.

(60) VahidMohammadi, A.; Moncada, J.; Chen, H.; Kayali, E.; Orangi, J.; Carrero, C. A.; Beidaghi, M. Thick and Freestanding Mxene/Pani Pseudocapacitive Electrodes with Ultrahigh Specific Capacitance. *J. Mater. Chem. A* **2018**, *6*, 22123–22133.

(61) Chenoweth, K.; van Duin, A. C. T.; Goddard, W. A. Reaxff Reactive Force Field for Molecular Dynamics Simulations of Hydrocarbon Oxidation. *J. Phys. Chem. A* **2008**, *112*, 1040–1053.

(62) Senftle, T. P.; Hong, S.; Islam, M. M.; Kylasa, S. B.; Zheng, Y.; Shin, Y. K.; Junkermeier, C.; Engel-Herbert, R.; Janik, M. J.; Aktulga, H. M.; Verstraelen, T.; Grama, A.; van Duin, A. C. T. The Reaxff Reactive Force-Field: Development, Applications and Future Directions. *npj Comput. Mater.* **2016**, *2*, 15011.

(63) Osti, N. C.; Naguib, M.; Ostadhossein, A.; Xie, Y.; Kent, P. R. C.; Dyatkin, B.; Rother, G.; Heller, W. T.; van Duin, A. C. T.; Gogotsi, Y.; Mamontov, E. Effect of Metal Ion Intercalation on the Structure of Mxene and Water Dynamics on Its Internal Surfaces. *ACS Appl. Mater. Interfaces* **2016**, *8*, 8859–8863.

(64) Osti, N. C.; Naguib, M.; Ganeshan, K.; Shin, Y. K.; Ostadhossein, A.; van Duin, A. C. T.; Cheng, Y.; Daemen, L. L.; Gogotsi, Y.; Mamontov, E.; Kolesnikov, A. I. Influence of Metal Ions Intercalation on the Vibrational Dynamics of Water Confined between Mxene Layers. *Physical Review Materials*. **2017**, *1*, 065406.

(65) Ganeshan, K.; Shin, Y. K.; Osti, N. C.; Sun, Y.; Prenger, K.; Naguib, M.; Tyagi, M.; Mamontov, E.; Jiang, D.-e.; van Duin, A. C. T. Structure and Dynamics of Aqueous Electrolytes Confined in 2D-TiO<sub>2</sub>/Ti<sub>3</sub>C<sub>2</sub>T<sub>2</sub> MXene Heterostructures. *ACS Appl. Mater. Interfaces* **2020**, *12* (52), 58378–58389.